Available online at www.sciencedirect.com

SCIENCE DIRECT®

International Journal of Heat and Mass Transfer 47 (2004) 2755–2767

International Journal of HEAT and MASS TRANSFER

www.elsevier.com/locate/ijhmt

Flow pattern and heat transfer of swirling flows in cylindrical container with rotating top and stable temperature gradient

Reima Iwatsu [*]

Department of Mechanical Engineering, Tokyo Denki University, 2-2 Kanda-Nishikicho, Chiyoda-ku, Tokyo 101-8457, Japan

Received 26 February 2003; received in revised form 24 October 2003

Abstract

The flow pattern and the heat transfer characteristics of confined swirling flows of viscous incompressible fluid in an cylindrical container are numerically investigated in the axisymmetric flow regime under the Boussinesq assumption. The flows are driven by rotating the top cover at a constant angular speed and stable temperature difference is imposed between the top and bottom discs with the side walls thermally insulated. Steady state solutions are obtained for ranges of governing parameters, the Reynolds number Re, the Richardson number Ri in $10^2 \leqslant Re \leqslant 3 \times 10^3$ and $0 \leqslant Ri \leqslant 1.0$ at fixed values of the Prandtl number $Pr = 1.0$ and the cylinder aspect ratio $h = 1.0$. For the flows with small Ri, meridional main circulation resides in the entire container convecting the heat from top to bottom disc. When Ri is increased to $\mathrm{O}(10^0)$, horizontally layered structure appears with quiescent lower half and vertically linear distribution of the temperature prevailing in much of the bulk. At intermediate values of Ri, i.e. $Ri \sim \mathrm{O}(10^{-1})$, flow separation occurs on the bottom disc depending on the values of Re and Ri. The flow patterns are classified into several different types on the (Ri, Re) plane. The average Nusselt number $\overline{Nu}$ which reflects the change of the flow structure, is a monotonically decreasing function of Ri and an increasing function of Re. The torque coefficient C_T is also computed and found to be a mildly decreasing function of Ri for the parameters considered.

1. Introduction

Swirling flows of viscous homogeneous fluid confined in cylindrical geometries had been studied much in the past [1–21]. Confined flows driven by constantly rotating one of the top or bottom discs were, after the pioneering works by Vogel [1], Pao [2], Bertelà and Gori [3] and Lugt and Haussling [4], systematically studied by Escudier [5] by means of fluorescent dye visualization. His experimental results disclosed that axisymmetric bubbles are created on the axis of rotation in steady state flows and the regions where up to three bubbles occur are charted as flow state diagram on the governing parameter plane. Succeeding numerical investigations [6–12] basically reconfirms the previous experimental findings. These axisymmetric bubbles are interpreted as bubble type vortex breakdown [13–17] and in the present study, the terminology bubble is used also to designate the recirculating region created in the meridional plane. The physical mechanism of the vortex breakdown was discussed by Brown and Lopez [8] and a concise expression of criteria was proposed which rely on the production of a negative azimuthal vorticity component [8,11]. The stability of steady flows and the onset of oscillatory instability was analyzed by using the linear stability theory [18]. In more recent studies, rotating waves which appear in high Reynolds number unsteady flows are being investigated [19–21]. From dynamical systems point of view, some authors have proceeded to show interest in the mixing property of these breakdown bubbles [9].

Lugt and Abboud [6] conducted a numerical study on the influence of various parameters on the properties of

---

[*] Tel.: +81-35280-3373; fax: +81-35280-3568.
E-mail address: iwatsu@cck.dendai.ac.jp (R. Iwatsu).

0017-9310/$ - see front matter © 2004 Elsevier Ltd. All rights reserved.
doi:10.1016/j.ijheatmasstransfer.2003.11.032

Nomenclature

C_{T}	torque coefficient (Eq. (15))
g	gravity acceleration
h	cylinder aspect ratio ($h = H/R$)
H	height of cylindrical container
Nu	local Nusselt number ($Nu = \partial T/\partial z\|_{z=0 \text{ or } h}$)
$\overline{Nu}$	average Nusselt number ($\overline{Nu} = \frac{1}{\pi}\int_0^1 Nu(r)2\pi r\,\mathrm{d}r$)
Pr	Prandtl number ($Pr = \nu/\kappa$)
r	radial coordinate
R	radius of cylindrical container
Re	Reynolds number ($Re = R^2\Omega/\nu$)
Ri	Richardson number ($Ri = (\alpha\Delta T g/R\Omega^2)h^3$)
T	temperature
T_0	standard temperature
u_r	velocity component in r-direction
u_z	velocity component in z-direction
u_φ	velocity component in φ-direction
z	axial coordinate

Greek symbols

α	thermal expansion coefficient
Δt	discrete time interval
ΔT	temperature difference between top and bottom discs
κ	thermal diffusion coefficient
ν	kinematic viscosity coefficient
ρ	density
φ	azimuthal coordinate
ψ	meridional streamfunction (Eq. (1))
ω	vorticity component in φ-direction (Eq. (2))
Ω	constant angular speed of top rotating disc

these separation bubbles. In their study, especially the Prandtl, Rayleigh, and normally assumed to be negligibly small Eckert numbers are changed under weakly unstable thermal boundary conditions. Their series of computations indicated that the occurrence of separation bubbles are very sensitive to the change of these parameters. The thermal effects on vortex breakdown is examined for fluid confined in a rotating concentric spherical annulus by Arkadyev et al. [22]. In the geometry of spherical gap container, depending on the relative strength of the imposed temperature difference and rate of rotation, the flow field shows various types of flow pattern: bubble type vortex breakdown, a vortex ring, or the development of recirculating zone near the outer sphere. The behavior of vortex breakdown bubbles under the influence of gravitationally stable and unstable situation in the cylindrical geometry is treated by Lee and Hyun [23]. In their numerical study, the applicability of the argument of Brown and Lopez is suggested which is based on the inviscid-kinematics, to the descriptions of the stagnation bubble in a stratified fluid. By comparing the relative magnitude of the terms in azimuthal vorticity equation, dominance of conduction is displayed for the Prandtl number $Pr \ll 1$, when the Richardson number $Ri > 0$, for large Pr, prevalence of convection is shown. Swirling flows under a gravitationally stable stratification in a cylinder is studied by Kim and Hyun [24]. Local Nusselt number at top and bottom discs is computed and its augmentation which is controlled by convective heat transport is discussed in their computation performed for cylinder with $h = 2.0$.

In the configuration under consideration in the present study, the temperature of the top disc is maintained higher than that of the bottom disc. Relative strength of the buoyancy due to stable temperature stratification and the convection of fluid driven by the rotating top disc is represented either in terms of the Grashof number Gr or the Richardson number Ri ($= Gr \times Re^{-2}$). As stated by [23], in the absence of the rotation of the disc, the fluid is at rest with hydrostatic pressure and linear temperature distribution developed in the vertical direction. Primary effect of the increased Ri is therefore to simplify the flow and temperature field toward the evident solution of the linear equations except for thin Ekman layer formed on the top boundary and Stewartson layer on the side wall. However, for intermediate values of Ri, the flow pattern is determined by the balance of centrifugal, Coriolis and vertical buoyancy forces all participating in the momentum equations. Predicting flow pattern is not an obvious task. Associated behavior of heat transfer characteristics is of interest which is represented by the average Nusselt number $\overline{Nu}$ as both Re and Ri are varied. The behavior of the torque coefficient C_{T} as Ri is increased might be also of applicational value to the engineering problems. Present computation is motivated by obtaining insight into the behavior of the flow at moderate values of Ri, and information on $\overline{Nu}$ and C_{T} whose values were not reported in the previous studies as Ri and Re encompass wide ranges of parameter space. Numerical solutions are obtained for the case of $Pr = \mathrm{O}(1)$ and a cylinder with same extent of radial and vertical length, i.e. $h = 1.0$. For cylinders with $h < 1.2$, the phenomenon of vortex breakdown is not relevant [5], however it will be shown in the present study that meridional secondary flow reveals flow separation on the lower boundary as well as on the axis depending on the values of Ri and Re.

2. Numerical method

2.1. Governing equations

The governing equations are the continuity equation, the momentum equations and the energy equation of the incompressible fluid under the Boussinesq assumption. In the present study, the axisymmetry of the flow is assumed and the vorticity–streamfunction procedure is utilized in the numerical computation. The meridional streamfunction ψ defined as

$$u_r = -\frac{1}{r}\frac{\partial\psi}{\partial z}, \qquad u_z = \frac{1}{r}\frac{\partial\psi}{\partial r} \tag{1}$$

and the azimuthal component of the vorticity ω given by

$$\omega \equiv \omega_\varphi = \frac{\partial u_r}{\partial z} - \frac{\partial u_z}{\partial r} \tag{2}$$

satisfy the elliptic equation

$$\frac{1}{r}\frac{\partial^2\psi}{\partial z^2} + \frac{\partial}{\partial r}\left(\frac{1}{r}\frac{\partial\psi}{\partial r}\right) = -\omega. \tag{3}$$

The vorticity transport equation

$$\begin{aligned}&\frac{\partial\omega}{\partial t} + \frac{\partial}{\partial r}(u_r\omega) + \frac{\partial}{\partial z}(u_z\omega) - \frac{1}{r}\frac{\partial u_\varphi^2}{\partial z}\\ &\quad = \frac{1}{Re}\left(\frac{\partial}{\partial r}\left(\frac{1}{r}\frac{\partial r\omega}{\partial r}\right) + \frac{\partial^2\omega}{\partial z^2}\right) - Ri\frac{\partial T}{\partial r},\end{aligned} \tag{4}$$

the azimuthal momentum equation

$$\begin{aligned}&\frac{\partial u_\varphi}{\partial t} + \frac{\partial}{\partial r}(u_r u_\varphi) + \frac{\partial}{\partial z}(u_z u_\varphi) - \frac{2u_r u_\varphi}{r}\\ &\quad = \frac{1}{Re}\left(\frac{\partial}{\partial r}\left(\frac{1}{r}\frac{\partial r u_\varphi}{\partial r}\right) + \frac{\partial^2 u_\varphi}{\partial z^2}\right)\end{aligned} \tag{5}$$

and the energy equation

$$\begin{aligned}&\frac{\partial T}{\partial t} + \frac{\partial}{\partial r}(u_r T) + \frac{\partial}{\partial z}(u_z T) - \frac{u_r T}{r}\\ &\quad = \frac{1}{RePr}\left(\frac{\partial}{\partial r}\left(\frac{1}{r}\frac{\partial T}{\partial r}\right) + \frac{\partial^2 T}{\partial z^2}\right)\end{aligned} \tag{6}$$

completes the system of equations. Above Eqs. (1)–(6) are solved for ψ, ω, u_φ and T. The second-order finite difference schemes on non-uniform grid are used throughout for the spatial discretization. No upwinding schemes are utilized. As to the time-marching, the second-order Adams–Bushforth scheme is used for the convection terms and the Crank–Nicolson scheme is used for the diffusion terms. Implicit equations are solved by the approximate factorization method. The Poisson equation for ψ and ω is iteratively solved by the conventional Red–Black–SOR method.

Reference scale for the length, time, velocity and pressure are R, Ω^{-1}, $R\Omega$ and $\rho R^2\Omega^2$ respectively. Dimensional temperature T^* is non-dimensionalized as $(T^* - T_0)/\Delta T$. After the non-dimensionalization, the physical parameters which govern the fluid motion and the temperature distribution are the rotational Reynolds number

$$Re = \frac{R^2\Omega}{\nu}, \tag{7}$$

the Richardson number

$$Ri = \frac{Gr}{Re^2} = \frac{\alpha\Delta T g H^3}{\nu^2}\frac{\nu^2}{R^4\Omega^2} = \frac{\alpha\Delta T g}{R\Omega^2}h^3, \tag{8}$$

the Prandtl number

$$Pr = \frac{\nu}{\kappa} \tag{9}$$

and the radius to height cylinder aspect ratio

$$h = \frac{H}{R}. \tag{10}$$

2.2. Boundary conditions and initial condition

The boundary conditions for the axisymmetric swirling flows in terms of ψ, ω, u_φ and T are (see Fig. 1), on the axis

$$\psi = 0, \quad \omega = 0, \quad u_\varphi = 0, \quad \frac{\partial T}{\partial r} = 0 \quad (r = 0, 0 \leqslant z \leqslant h), \tag{11}$$

on the side wall

$$\psi = 0, \quad \omega = -\frac{\partial^2\psi}{\partial r^2}, \quad u_\varphi = 0, \quad \frac{\partial T}{\partial r} = 0 \quad (r = 1, 0 \leqslant z \leqslant h), \tag{12}$$

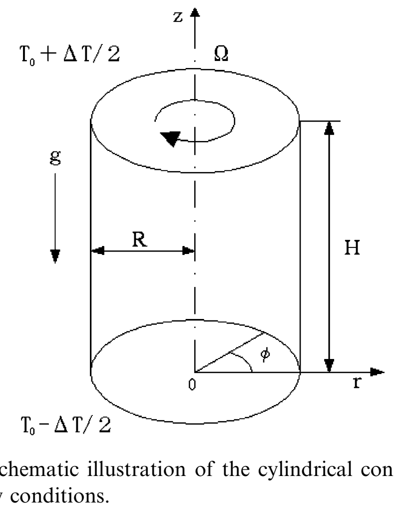

Fig. 1. Schematic illustration of the cylindrical container and boundary conditions.

on the bottom disc

$$\psi = 0, \qquad \omega = -\frac{1}{r}\frac{\partial^2\psi}{\partial z^2}, \qquad u_\varphi = 0, \qquad T = -0.5 \quad (z = 0, 0 \leqslant r \leqslant 1), \tag{13}$$

and on the rotating top disc

$$\psi = 0, \qquad \omega = -\frac{1}{r}\frac{\partial^2\psi}{\partial z^2}, \qquad u_\varphi = r, \qquad T = 0.5 \quad (z = h, 0 \leqslant r \leqslant 1). \tag{14}$$

The derivatives on the boundaries are evaluated by the second-order one-sided finite difference scheme.

The initial condition for each run is the conductive solution of the heat transfer equation: the fluid is at rest and the temperature variation is vertically linear. The computation is continued until convergence criteria of $(\psi^n - \psi^{n-1})/\Delta t \leqslant 5 \times 10^{-7}$ and $(P^n - P^{n-1})/\Delta t \leqslant 10^{-5}$ are satisfied. In the above equations, P denotes the value of z and r coordinate of stagnation points on the axis and bottom, if there exists any. These values are calculated by searching for the zeros of w on the axis and u on the bottom disc respectively. The second criterion assures that the convergence is complete and no oscillation is observed in the dividing streamlines on the meridional plane. Otherwise the computation is carried out up to non-dimensional time of $t = 6000$. Typical value of time stepping increment Δt was 5×10^{-3}, though as small value as 5×10^{-4} was necessary for some cases at low Re.

Prior to parametric computation, the grid-dependence of the present numerical method is checked for representative value of parameters. The result of this test is shown in Table 1. The value of the average Nusselt number is obtained by taking the average of $\overline{Nu}$ calculated at top and bottom discs. Numerical error in these values, $\overline{Nu}(z = 0)$ and $\overline{Nu}(z = h)$ is at most 2% when $(Re, Ri) = (3 \times 10^3, 0)$ and in many cases, less than 0.8%. According to Table 1, while the maximum value of the streamfunction, the average Nusselt number and torque coefficient differ 3%, 1% and 6% respectively between the coarse and medium grid, differences between the medium and fine grid are only 0.7% 0.5% and 8% respectively. The graphical output of streamlines and isotherms for these two solutions exhibits identical plots when visually inspected. According to the outcome of this test, although the torque coefficient is quantitatively sensitive to the grid resolution, the grid with medium number of grid points, i.e. $n_r \times n_z = 81 \times 81$ is considered to have sufficient resolution for the present purpose and medium grid is used in the following computation. For the medium grid, the minimum and maximum grid spacing are 4.41×10^{-3} and 1.98×10^{-2} respectively. Parametric computation was carried out on a personal computer with Celeron 2 GHz cpu and the cpu-time per a typical case was about 3 h.

3. Results and discussion

Numerical solutions are obtained for fluid with $Pr = 1.0$, enclosed in a cylindrical container with the radius to height aspect ratio $h = 1.0$. The Reynolds number and the Richardson number are varied in ranges of $10^2 \leqslant Re \leqslant 3 \times 10^3$ and $0 \leqslant Ri \leqslant 1.0$. For the parameters covered in the present study, steady solutions are obtained (cf., e.g. [18]). Of particular interest in this cylindrical geometry has been the occurrence of vortex breakdown phenomenon in the past literatures. According to the experimental visualization of homogeneous fluid, symmetric bubble type vortex breakdown is known to occur for the cylinder aspect ratio $h \geqslant 1.2$ [5]. In the present numerical simulation carried out for a cylinder with $h = 1.0$ and $Ri = 0$, no bubble is created on the rotation axis in accordance with the past experimental as well as numerical studies. However, close observation of the streamline plots reveals that although flow reversal does not occur along the axis in the axial direction, concave surface is created in stream surfaces surrounding the axis of rotation when Re exceeds ca. 8×10^2 and continues to exist when Re is further increased. A marked change of the meridional flow pattern is observed when Ri is increased to a value of $Ri \sim O(10^{-1})$ where meridional main circulation is concentrated in radially outer region $(0.5 < r < 1)$ and flow separation occurs on the bottom stationary disc.

3.1. Velocity and temperature distribution

Let us first examine the effect of Ri on the flow field by comparing the case with minor influence of buoyancy and that with substantial buoyancy force. Contour plots of streamfunction ψ, vorticity ω, azimuthal velocity component u_φ and isotherms are shown in (a)–(d) of Figs. 2–5 for two extreme values of Ri, i.e. $Ri = 0$ and 1.0. When $Ri = 0$ and Re is low, the rotating top cover drags the fluid and stirs swirling motion near the top disc

Table 1
Comparison of solutions with different grid resolution ($Re = 10^3$, $Ri = 0$, $Pr = 1.0$ and $h = 1.0$)

Grid	$n_r \times n_z$	$\psi_{\max}$	$\psi_{\min}$	$\overline{Nu}$	C_T
Coarse	41×41	9.96×10^{-3}	-2.51×10^{-7}	5.805	11.2
Medium	81×81	9.71×10^{-3}	-1.59×10^{-7}	5.736	11.9
Fine	161×161	9.64×10^{-3}	-1.29×10^{-7}	5.708	12.8

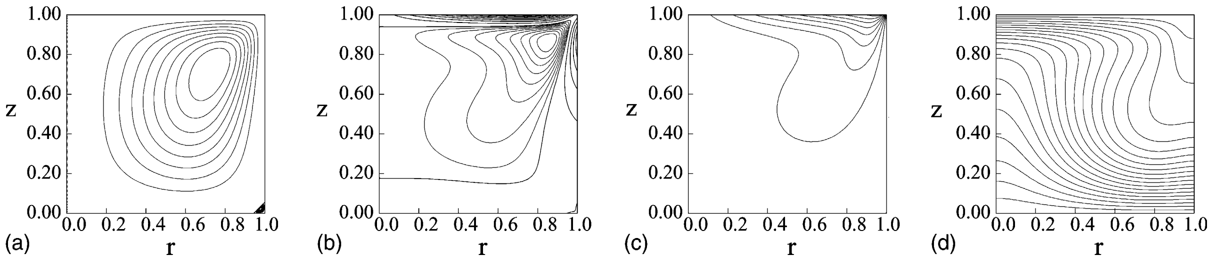

Fig. 2. Contour plots of streamfunction ψ, azimuthal vorticity component ω, azimuthal velocity component u_φ and isotherms. Contour values are (a) $\psi = (i/10)^3\psi_{\max}, i = 0,\dots,10$, $\psi = (i/10)^3\psi_{\min}, i = 0,\dots,10$, (b) $\omega = (i/10)^3\omega_{\max}, i = 0,\dots,10$, $\omega = (i/10)^3\omega_{\min}$, $i = 0,\dots,10$, (c) $u_\varphi = (i/10), i = 0,\dots,10$, and (d) $T = (i/20), i = 0,\dots,20$. $Re = 3 \times 10^2$, $Ri = 0$, $Pr = 1.0$ and $h = 1.0$.

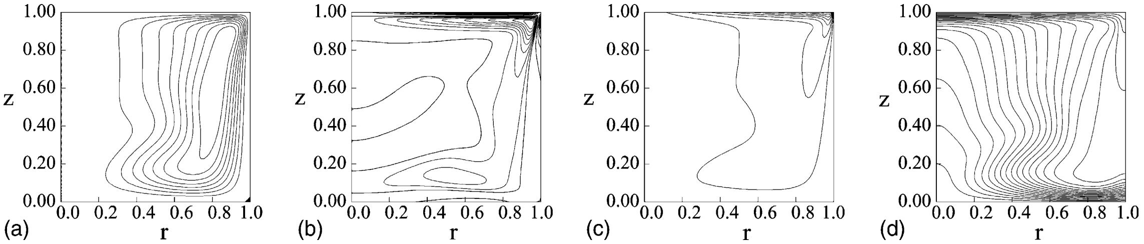

Fig. 3. Similar plots for $Re = 2 \times 10^3$, $Ri = 0$, $Pr = 1.0$ and $h = 1.0$.

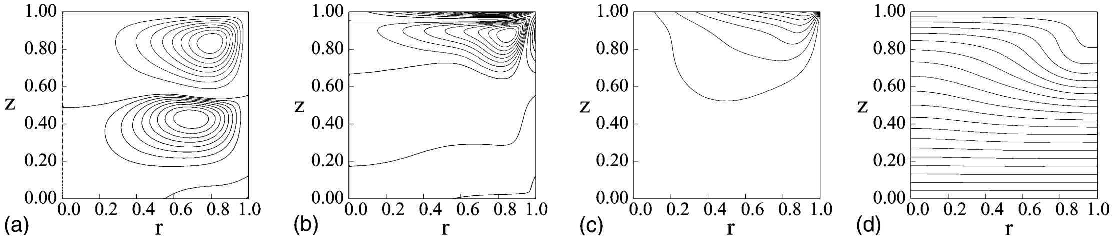

Fig. 4. Similar plots for $Re = 3 \times 10^2$, $Ri = 1.0$, $Pr = 1.0$ and $h = 1.0$.

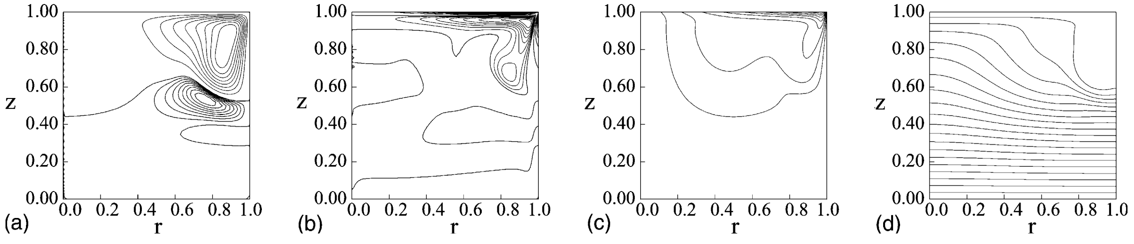

Fig. 5. Similar plots for $Re = 2 \times 10^3$, $Ri = 1.0$, $Pr = 1.0$ and $h = 1.0$.

owing to the viscous stress as exhibited by the contour lines of u_φ in Fig. 2(c). A circulating cell is created in the meridional plane (r, z) as a result of the dynamic interaction between the swirling component and the meridional components by the action of centrifugal force and Coriolis force (Fig. 2(a)). Isotherms in Fig. 2(d) exhibit that although almost equi-spaced contours are seen in the vicinity of top and bottom walls, a horizontal temperature gradient exists in the bulk of the container. When Re is high (Fig. 3), thin boundary layers are visible in the plots of u_φ. The vertical contour lines near the axis are suggesting that the axial component of the vorticity ω_z is close to constant whose value is by rough estimation about $\Omega/4$. This is qualitatively in agreement with the bulk flow of the Batchelor's solution for infinite discs [25,26]. Main circulating cell occupies the whole (r,z) plane as it was in the low Re flows. It is noticed that the stream lines run almost parallel to z-axis in the vicinity of the axis indicating $u_r \sim 0$, $\frac{\partial u_z}{\partial z} \sim 0$, thus $\omega_\varphi \sim 0$ in this region in high Re flows. Isotherms are more clustered near the top and bottom boundaries and temperature gradient in the bulk of the fluid body tends to be radial rather than vertical.

The effect of buoyancy is distinctively seen in Figs. 4 and 5 with $Ri = 1.0$. When $Re = 3 \times 10^2$, the swirling motion is more confined in the vicinity of the upper rotating wall as seen in Fig. 4(c). Meridional flow displays upper larger circulating cell and lower smaller recirculating cell (Fig. 4(a)). In these plots of streamfunction, the values of contours are not equi-spaced so that care must be taken when interpreting the strength of these recirculations not to overestimate the strength of recirculating cells. Isotherms are more horizontal than it is in Fig. 2(d) and vertical gradient in the whole container appears to be almost constant. When $Re = 2 \times 10^3$ (Fig. 5), similar tendency is observed as in the plots for $Re = 3 \times 10^2$. The azimuthal component of the velocity u_φ exhibits thin boundary layer at the top wall and the magnitude of u_φ in lower portion of the container is virtually null. However, closer examination reveals that contour lines in the vicinity of the top disc boundary layer is almost vertical near the axis ($r < 0.3$), indicating that fluid layer of considerable depth (approximately $0.8 < z$) is rotating rigidly. Meridional circulation is almost stagnant in this region. This rigid rotation of the fluid layer is conspicuous when $Ri \geqslant 0.5$. Intense meridional motion is confined in the upper half ($0.5 \geqslant z$), close to the side wall ($0.5 \leqslant r$) region (Fig. 5(a)). Circulating cell is observed near the top right corner and induced recirculating cells are horizontally stretched forming a horizontally layered structure. In this region near the top and side walls, the fluid is well mixed and the temperature is relatively higher than the ambient fluid at the same height (Fig. 5(d)).

In order to illustrate the influence of buoyancy force on the vertical velocity distribution in a more clear manner, velocity components are plotted along a vertical line at $r = 0.8$ for $Ri = 0$ and 1.0, $Re = 3 \times 10^2$ and 2×10^3 in Fig. 6. In Fig. 6(b), (d) and (f), additional data is shown for $Ri = 3.0$. It is noted first that the magnitude of u_φ decreases substantially in the portion $z < 0.6$ for both low and high Reynolds number cases as shown in Fig. 6(c) and (d) when Ri is increased to unity. For the high Re case plotted in Fig. 6(d), u_φ plot displays thin boundary layer in the vicinity of top disc, a well mixed layer of fluid with constant value of u_φ in upper portion of the container, $0.6 < z < 1$, and diminishingly small values in lower portion $z < 0.6$. When Ri is further increased to 3.0, the influence of the disc rotation penetrates smaller distance from the top boundary. Similar trend is seen in the plots of u_r and u_z in Fig. 6(a), (b) and (e), (f). In all figures shown above, it is observed that the effect of externally imposed temperature gradient inhibits the vertical motion and the swirling motion tends to be confined in shallower depth near the rotating boundary as Ri is increased.

Temperature distribution plotted in Fig. 7 for the same values of Re and Ri displays similar trend that is consistent with the previous velocity profiles. As Ri is increased to $\mathrm{O}(1)$, temperature over most of the depth becomes a linear function of z, i.e. $T \propto z$, with its inclination approaches toward unity (see Fig. 7(b)) suggesting that the local Nusselt number at top and bottom discs also approaches toward unity. Above comparison of flows at $Ri = 0$ and 1.0 thus discloses the changeover of convective meridional main circulation to the circulation localized in a shallow layer adjacent to the top disc, and convective to conductive temperature distribution.

The flow structure at medium values of Ri, i.e. $Ri \sim \mathrm{O}(10^{-1})$ is exemplary shown next in Fig. 8 for $Re = 2 \times 10^3$ and $Ri = 7 \times 10^{-2}$. The value of u_φ becomes smaller in the lower part of container ($z \sim 0.2$) as compared with the flow at $Ri = 0$, however it is interesting to observe that the value of u_φ is increased in the portion near the top disc ($r \sim 0.4$, $z \sim 0.8$). Similar tendency is more clearly seen in the portion near the top disc and axis ($r < 0.3$, $z > 0.8$) of the plots for $Ri = 1.0$ in Fig. 5(c). Decreased value of u_φ in the lower half of the container is a straightforward consequence of the action of vertical buoyancy force, though another interesting observation is that the meridional main circulation tends to be shifted toward radially outward portion ($r > 0.5$) of the cylinder, leaving radially inward portion ($r < 0.5$) almost stagnant (Fig. 8(a)). This trend becomes gradually obvious as Ri exceeds ca. 5×10^{-2} and $Re \geqslant 10^3$. Although the streamlines are concentrated in radially outer half of the cylinder, the strength of this main circulation at $Ri = 7 \times 10^{-2}$ still retains substantial magnitude, as will be shown in Fig. 9. In the lower portion of the streamlines, a mild concave surface is seen. Compared with Fig. 5(b) for $Ri = 1.0$, the contour plots of ω in Fig. 8(b) exhibits smaller (negative) value in this region. It is plausible that the horizontal temperature gradient at medium value of Ri contributes in the production of negative azimuthal vorticity. A separation bubble is seen to be created on the surface of bottom disc at $r \sim 0.6$. Separation on the bottom disc is observed for the flows with $Ri \geqslant 6 \times 10^{-2}$ and $Re \geqslant 9 \times 10^2$.

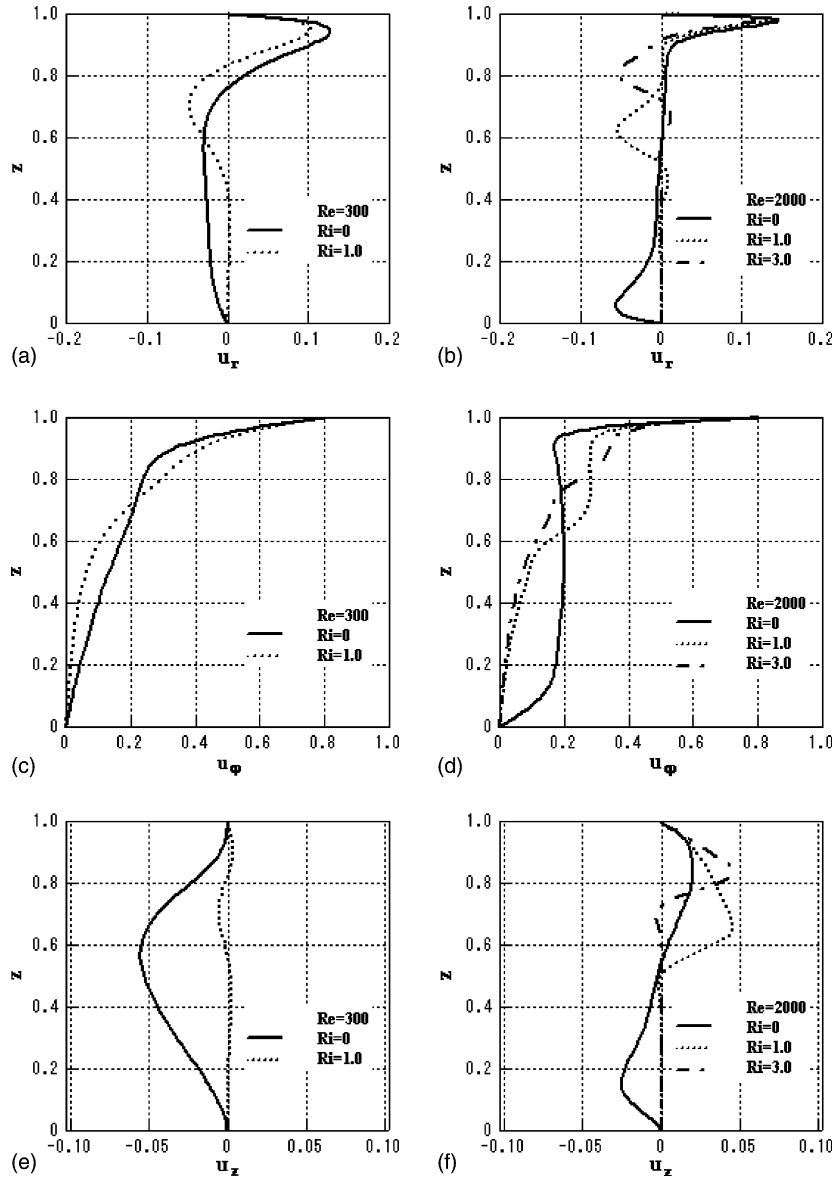

Fig. 6. Plots of velocity components along a vertical line at $r = 0.8$. (a) u_r for $Re = 3 \times 10^2$, (b) u_r for $Re = 2 \times 10^3$, (c) u_φ for $Re = 3 \times 10^2$, (d) u_φ for $Re = 2 \times 10^3$, (e) u_z for $Re = 3 \times 10^2$, and (f) u_z for $Re = 2 \times 10^3$.

3.2. Magnitude of meridional streamfunction

Local maximum value of the streamfunction $\psi_{\max}$ and location of points on the meridional plane where $\psi = \psi_{\max}$ are then shown in Fig. 9 as a function of Ri for $Re = 10^2$, 3×10^2, 10^3 and 2×10^3. Similar plots for the minimum of the streamfunction $\psi_{\min}$ are shown in Fig. 10. $\psi_{\max}$ indicates the volumetric flow rate of meridional main circulation and its location, the center of circulating cell, $\psi_{\min}$ the volumetric flow rate of recirculating cell and its location, the center of recirculating cell respectively. In the present computation, the value of $\psi_{\max}$ at a fixed value of Ri increases when $10^2 \leqslant Re \leqslant 2 \times 10^2$ and gradually decreases when $Re \geqslant 3 \times 10^2$. On the other hand, for all Re cases shown in Fig. 9(a), $\psi_{\max}$ is a decreasing function of Ri. The location of the points where ψ attains maximum is shown in Fig. 9(b). For each Re, a point with smallest value of r and z corresponds to the case of $Ri = 0$ and largest value of r and z corresponds to the case of $Ri = 1.0$. All the points plotted in the right upper half of the meridional plane display similar tendency as Ri

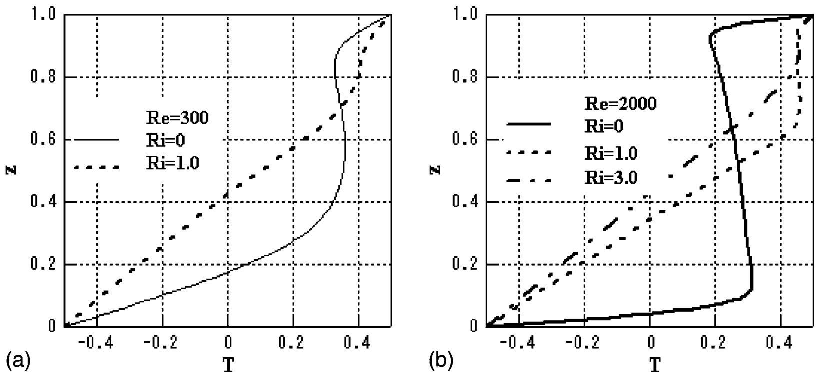

Fig. 7. Temperature profile along a vertical line at $r = 0.8$. (a) $Re = 3 \times 10^2$ and (b) $Re = 2 \times 10^3$.

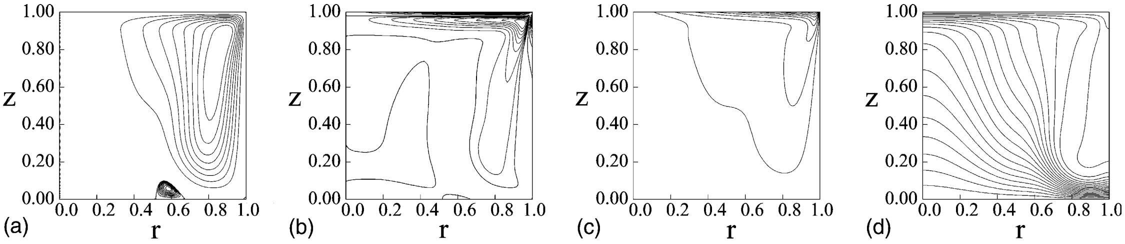

Fig. 8. Similar plots to Fig. 2 except for $Re = 2 \times 10^3$, $Ri = 7 \times 10^{-2}$, $Pr = 1.0$ and $h = 1.0$.

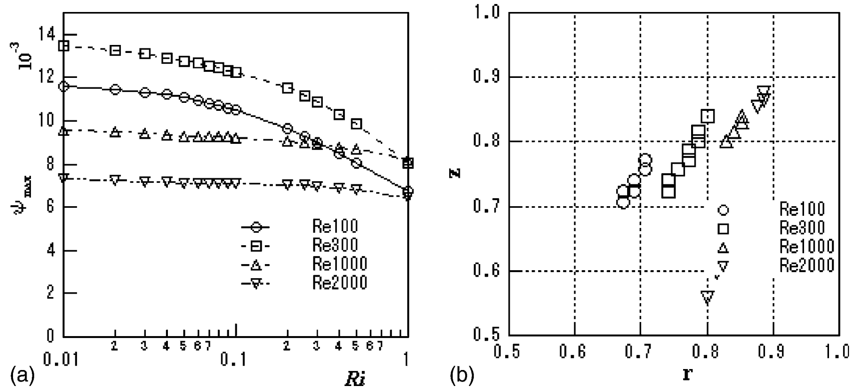

Fig. 9. Local maximum value of the streamfunction. (a) $\psi_{\max}$ versus Ri. (b) Location where ψ is maximum, plotted on the meridional plane (r, z).

is increased, i.e. the center of the main circulating cell moves toward the right upper corner at $(r, z) = (1, h)$. In these figures, decreased meridional flow rate and localized meridional circulation in the vicinity of the top disc as Ri is increased are clearly indicated.

Similar plots for $\psi_{\min}$ in Fig. 10(a) exhibit that when Ri is increased, magnitude of $\psi_{\min}$ is virtually zero for up to a certain value of the order $Ri \sim O(10^{-1})$ and then increases as Ri. This is indicative that when Ri reaches to a certain value ($Ri = 0.1$ in case $Re = 4 \times 10^2$ and $Ri = 0.07$ in case $Re = 3 \times 10^3$), flow separation occurs and this critical value for separation varies as Re is varied. The magnitude of $\psi_{\min}$ is still increasing at $Ri = 1.0$, however the present computation covers only a finite range of Ri and therefore if Ri is increased to extremely large value, both $\psi_{\max}$ and $\psi_{\min}$ are considered to decrease ultimately and diminishes toward zero because of the strong restriction of vertical motion due to the

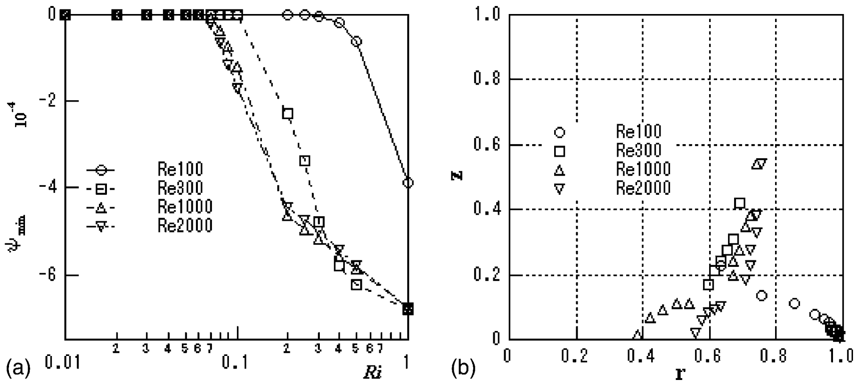

Fig. 10. Local minimum value of the streamfunction. (a) ψ_{min} versus Ri. (b) Location where ψ is minimum, plotted on the meridional plane (r, z).

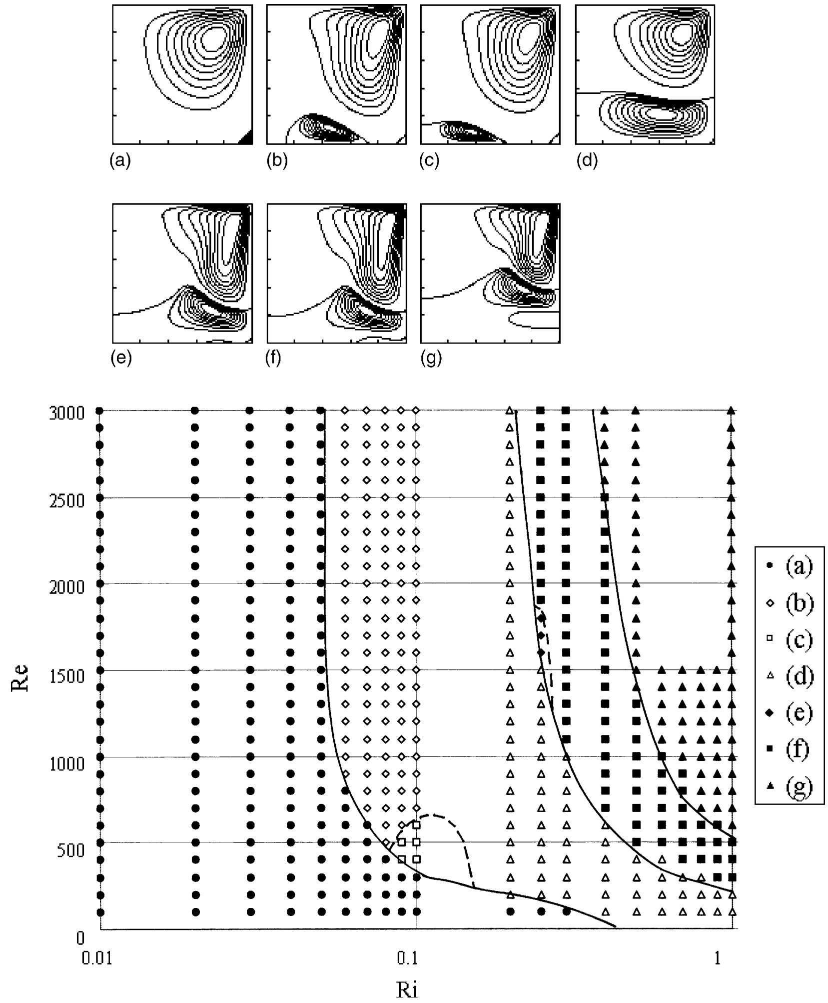

Fig. 11. Flow pattern diagram on (Ri, Re) plane. Re and Ri for the inset are (a) $Re = 200$, $Ri = 0.1$, (b) $Re = 700$, $Ri = 0.1$, (c) $Re = 500$, $Ri = 0.1$, (d) $Re = 300$, $Ri = 0.25$, (e) $Re = 1700$, $Ri = 0.25$, (f) $Re = 2000$, $Ri = 0.25$, and (g) $Re = 1000$, $Ri = 0.8$.

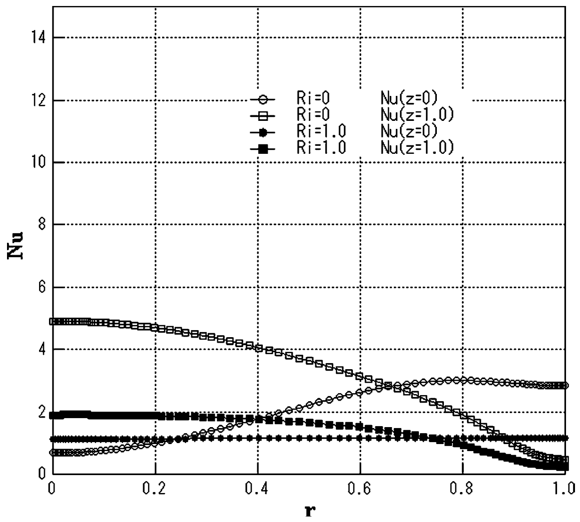

Fig. 12. Local Nusselt number *Nu* at top and bottom discs. $Re = 3 \times 10^2$, $Pr = 1.0$ and $h = 1.0$.

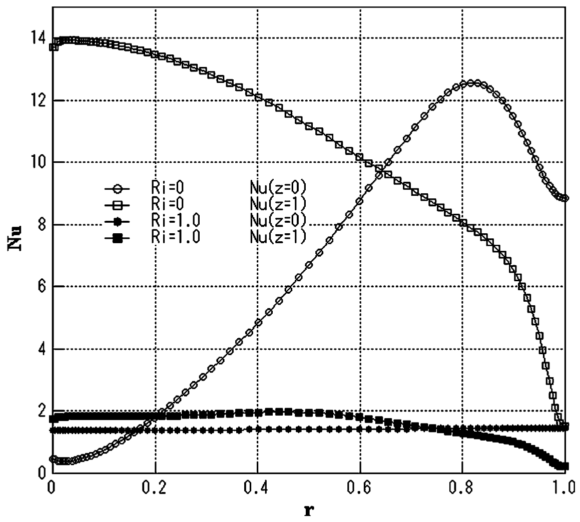

Fig. 13. Local Nusselt number *Nu* at top and bottom discs. $Re = 2 \times 10^3$, $Pr = 1.0$ and $h = 1.0$.

buoyancy force. The location of $\psi_{\min}$ as plotted in Fig. 10(b) shows that when $Re = 10^2$, the corner bubble which originally dwells at the bottom right corner grows its size and finally occupies the lower half of the container as *Ri* is increased. Contrary to the behavior at low *Re*, two rows of points for $Re = 10^3$ and 2×10^3 are indicating that a recirculating bubble is created on the bottom boundary and then this bubble grows in size and migrates toward the side wall as *Ri* is increased.

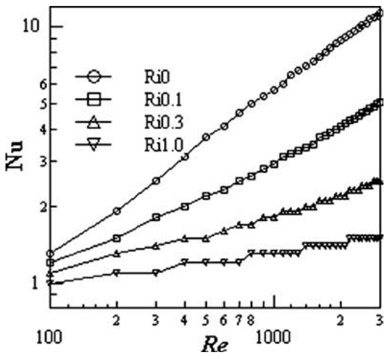

Fig. 14. Average Nusselt number $\overline{Nu}$ as functions of *Re*.

3.3. Flow patterns

Flow patterns are classified into several types according to the arrangement and number of meridional recirculating cells in Fig. 11. The definition of the types are explained in the inset of the figure. When *Ri* is small, the effect of the buoyancy is negligibly small, single main circulating cell is developed in the whole meridional plane with a minor corner separation slightly visible in the right lower corner between the side wall and the bottom disc (type a). When *Ri* is increased to $Ri \geqslant \mathrm{O}(1)$, the effect of thermal stratification is substantial, horizontally layered pattern emerges with main circulating cell near the top rotating disc and horizontally stretched secondary recirculating cells induced (types d–g). In between these two extreme cases, i.e. $Ri \sim \mathrm{O}(10^{-1})$, main circulation tends to be confined in radially outer portion ($r > 0.5$) and several flow patterns are noted in a small region of (Ri, Re) plane, e.g. separation bubble created on the bottom disc (type b) and corner bubble created between the axis and the bottom disc (type c) when $(Ri, Re) \sim (0.1, 500)$. The influence of *Re* on the flow pattern is palpable, however it is restricted to the cases with $Re \leqslant 10^3$.

3.4. Nusselt number

Radial distribution of local Nusselt number $Nu(r)$ at top and bottom discs is shown in Figs. 12 and 13 for $Re = 3 \times 10^2$ and 2×10^3 respectively. Increased heat transfer owing to the convective fluid motion is noted by comparing the plots for low and high *Re* when $Ri = 0$. When *Ri* is increased to 1.0, profile of *Nu* exhibits a marked contrast to the previous plots for $Ri = 0$. Almost uniform distribution of *Nu* suggests the suppression of vertical fluid motion by the thermal stratification and thus large portion of heat transfer between the top and bottom boundaries is carried out by the conduction.

The average Nusselt number $\overline{Nu}$ is then shown first as a function of *Re* in Fig. 14 and as a function of *Ri* in

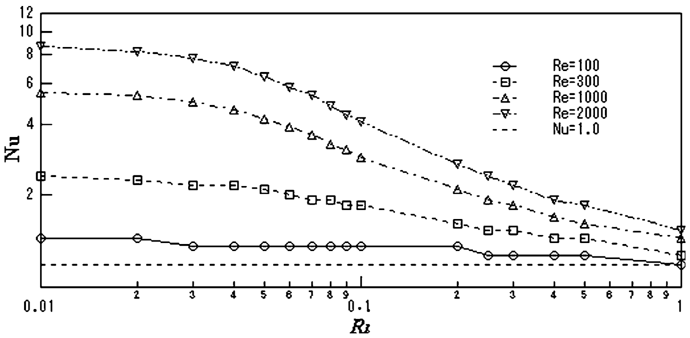

Fig. 15. Average Nusselt number $\overline{Nu}$ as functions of Ri.

Table 2
Correlation of average Nusselt number $\overline{Nu}$ with the Reynolds number Re: $\overline{Nu} = CRe^k$

Ri	0	0.01	0.02	0.03	0.04	0.05	0.06	0.07	0.08
k	0.643	0.636	0.624	0.607	0.586	0.560	0.532	0.504	0.447
C	0.0675	0.0684	0.0709	0.0749	0.0802	0.0881	0.0981	0.110	0.151
Ri	0.09	0.1	0.2	0.25	0.3	0.4	0.5	1.0	
k	0.449	0.426	0.295	0.263	0.236	0.201	0.180	0.112	
C	0.139	0.154	0.274	0.314	0.354	0.409	0.444	0.601	

Re is varied in a range $10^2 \leqslant Re \leqslant 3\times 10^3$, $Pr = 1.0$ and $h = 1.0$.

Fig. 15. Logarithmic plots in Fig. 14 exhibits fair degree of linearity between $\log Re$ and $\log \overline{Nu}$. The inclination of these lines decreases as Ri is increased. Correlation coefficients calculated for various Ri are given in Table 2.

Plots in Fig. 15 clearly exhibits a tendency that as Ri is increased, $\overline{Nu}$ gradually approaches to the limiting value of 1.0. Precise nature of the function which gives $\overline{Nu}$ as a function of Ri is unknown, however after some calculations we find that a relationship $\overline{Nu}(Ri) = [\overline{Nu}(Ri = 0) + Ri^2]/[1 + Ri^2]$ turned out to be a simple approximation of the computed curves.

Finally, complete information about $\overline{Nu}$ is given in Fig. 16 in which contour plots of $\overline{Nu}$ is constructed on the parameter plane (Ri, Re).

3.5. Torque coefficient

Of particular interest to engineering applications is the torque coefficient C_T necessary to sustain the top disc rotation. The torque coefficient in the present study is defined as

$$C_\mathrm{T} = \frac{1}{\pi}\int_0^1 \left.\frac{\partial u_\varphi}{\partial z}\right|_{z=h} 2\pi r^2\,\mathrm{d}r. \tag{15}$$

According to the present numerical computation, C_T is an increasing function of Re (Fig. 17). The torque obtained for the enclosed fluid with $Ri = 0$ in the present study is substantially larger than that obtained by the similarity solution for one side of the disc placed in fluid of infinite expanse [25,26]. In the present case of fluid confined in a finite container, the vorticity component ω_φ is not restricted to a thin layer and this distributed vorticity should contribute to an increased torque value through dynamic interaction of three components of the vorticity equation. When $Re \geqslant 10^3$, the following

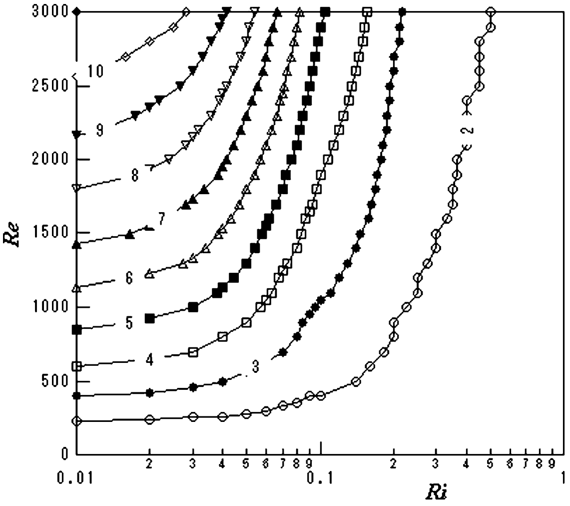

Fig. 16. Contour plots of average Nusselt number $\overline{Nu}$ on the parameter plane (Ri, Re).

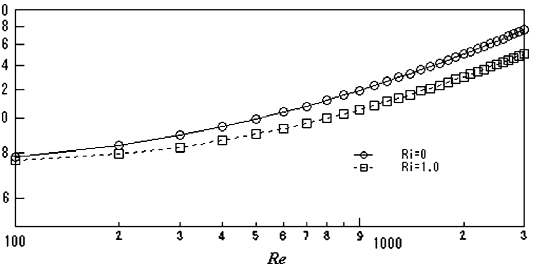

Fig. 17. Torque coefficient C_T as a function of Re. $Ri = 0$ and 1.0, $Pr = 1.0$ and $h = 1.0$.

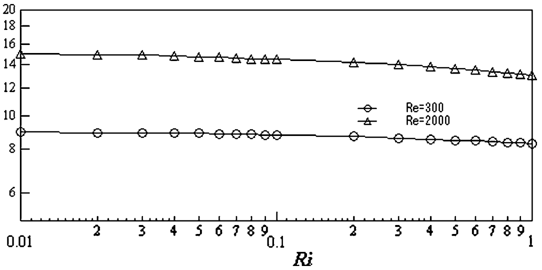

Fig. 18. Torque coefficient C_T as a function of Ri. $Re = 3 \times 10^2$ and 2×10^3, $Pr = 1.0$ and $h = 1.0$.

equations are found to hold approximately: $C_T(Ri = 0) \propto Re^{0.35}$ and $C_T(Ri = 1.0) \propto Re^{0.32}$. The value of C_T slightly decreases when Ri is increased over the parameter range covered in the present computation (Fig. 18). Technical inference of the present result might be that it may be possible to control the magnitude of torque by appropriately imposing a vertical thermal boundary condition on to engineering devices which enclose rotating fluid as working fluid within the container.

4. Conclusions

The effect of stable temperature gradient on swirling flows confined in a cylindrical container is numerically investigated for wide ranges of governing parameters Re and Ri at fixed values of $Pr \sim 1.0$ and $h \sim 1.0$. When Ri is increased to O(1), horizontally layered structure emerges. Plotted isotherms exhibit variation of the convection dominated solution to the conduction dominated solution of linear equations as Ri is increased. Interesting findings are for the intermediate values of Ri, i.e. $Ri \sim O(10^{-1})$, meridional circulation is concentrated in radially outer portion of the cylinder ($r > 0.5$) and flow separation occurs on the bottom boundary. Several flow patterns are developed depending on the values of Ri and Re, e.g. separation bubble on the bottom disc, corner bubble at the corner between the axis and the bottom disc, and corner separation at the corner between the bottom disc and sidewall. Finally the average Nusselt number $\overline{Nu}$ and the torque coefficient C_T are computed as functions of Re and Ri. Above numerical results are open for experimental validation and cross comparison of numerical and experimental output should deepen the understanding of the fluid flow under consideration.

Acknowledgements

The author thanks Prof. J.M. Hyun for discussions during his visit to TDU.

References

[1] H.U. Vogel, Experimentelle Ergebnisse über die laminare Strömung in einem zylindrischen Gehäuse mit darin rotierender Scheibe, Max-Planck-Institut für Strömungsforschung, Bericht 6, 1968.
[2] H.P. Pao, A numerical computation of a confined rotating flow, Trans. ASME J. Appl. Mech. 37 (1970) 480–487.
[3] M. Bertelá, F. Gori, Laminar flow in a cylindrical container with a rotating cover, Trans. ASME J. Fluids Eng. 104 (1982) 31–39.
[4] H.J. Lugt, H.J. Haussling, Axisymmetric vortex breakdown in rotating fluid within a container, Trans. ASME J. Appl. Mech. 49 (1982) 921–923.
[5] M.P. Escudier, Observations of the flow produced in a cylindrical container by a rotating endwall, Exp. Fluids 2 (1984) 189–196.
[6] H.J. Lugt, M. Abboud, Axisymmetric vortex breakdown with and without temperature effects in a container with a rotating lid, J. Fluid Mech. 179 (1987) 179–200.
[7] J.M. Lopez, Axisymmetric vortex breakdown. Part 1: Confined swirling flow, J. Fluid Mech. 221 (1990) 533–552.
[8] G.L. Brown, J.M. Lopez, Axisymmetric vortex breakdown. Part 2: Physical mechanisms, J. Fluid Mech. 221 (1990) 553–576.
[9] J.M. Lopez, A.D. Perry, Axisymmetric vortex breakdown. Part 3: Onset of periodic flow and chaotic advection, J. Fluid Mech. 234 (1990) 449–471.
[10] N. Tsiverblit, Vortex breakdown in a cylindrical container in the light of continuation of a steady solution, Fluid Dyn. Res. 11 (1993) 19–35.
[11] J.P. Watson, G.P. Neitzel, Numerical evaluation of a vortex-breakdown criterion, Phys. Fluids 8 (11) (1996) 3063–3071.
[12] R. Iwatsu, H.S. Koyama, Numerical study of steady axisymmetric vortex breakdown in a cylindrical container (1st Report, limiting Reynolds number of the occurrence of vortex breakdown and the location of stagnation point), Trans. JSME/B 66 (643) (2000) 107–114 (in Japanese).
[13] M.G. Hall, Vortex breakdown, Ann. Rev. Fluid Mech. 4 (1972) 195–218.
[14] S. Leibovich, The structure of vortex breakdown, Ann. Rev. Fluid Mech. 10 (1978) 221–246.

[15] M. Escudier, Vortex breakdown: observations and explanations, Prog. Aerospace Sci. 25 (1988) 189–229.
[16] J.M. Delery, Aspects of vortex breakdown, Prog. Aerospace Sci. 30 (1994) 1–59.
[17] V. Shtern, F. Hussain, Collapse, symmetry breaking, and hysteresis in swirling flows, Ann. Rev. Fluid Mech. 31 (1999) 537–566.
[18] A.Yu. Gelfgat, P.Z. Bar-Yoseph, A. Solan, Stability of confined swirling flow with and without vortex breakdown, J. Fluid Mech. 311 (1996) 1–36.
[19] H.M. Blackburn, J.M. Lopez, Symmetry breaking of the flow in a cylinder driven by a rotating end wall, Phys. Fluids 12 (11) (2000) 2698–2701.
[20] F. Marques, J.M. Lopez, Processing vortex breakdown mode in an enclosed cylinder flow, Phys. Fluids 13 (6) (2001) 1679–1682.
[21] E. Serre, P. Bontoux, Vortex breakdown in a three-dimensional swirling flow, J. Fluid Mech. 459 (2002) 347–370.
[22] A. Arkadyev, P. Bar-Yoseph, A. Solan, Thermal effects on axisymmetric vortex breakdown in a spherical gap, Phys. Fluids A 5 (5) (1993) 1211–1223.
[23] C.H. Lee, J.M. Hyun, Flows of a stratified fluid in a cylinder with a rotating lid, Int. J. Heat Fluid Flow 20 (1999) 26–33.
[24] W.N. Kim, J.M. Hyun, Convective heat transfer in a cylinder with a rotating lid under stable stratification, Int. J. Heat Fluid Flow 18 (1997) 384–388.
[25] G.K. Batchelor, An Introduction to Fluid Dynamics, Cambridge University Press, London, 1967, 292 pp.
[26] H. Schlichting, Boundary-layer Theory, seventh (English) ed., McGraw-Hill Inc., New York, 1979, 106 pp.